



Tailoring electromechanical performance in BiScO₃-modified Bi_{0.5}Na_{0.5}TiO₃-based lead-free piezoceramics

Leijie Wang¹ · Wangfeng Bai² · Xinyu Zhao² · Yuqin Ding² · Fei Wen¹ · Lili Li¹ · Wei Wu¹ · Peng Zheng¹ · Jiwei Zhai³

Received: 27 September 2019 / Accepted: 28 November 2019 / Published online: 2 December 2019
© Springer Science+Business Media, LLC, part of Springer Nature 2019

Abstract

The strain response of lead-free ternary solid solution $(1-x)$ $(0.94 \text{ Bi}_{0.5}\text{Na}_{0.5}\text{TiO}_3-0.06\text{BaTiO}_3)-x\text{BiScO}_3$ (BNT–BT–BS) have been tailored by controlling the phase transition temperature. The effects of BiScO₃ on the phase structure, dielectric, ferroelectric, piezoelectric properties, and electric field-induced strain are systematically investigated. A schematic phase diagram has also been established to clarify the relationship between strain behavior and structure evolution. The field-induced strain increases progressively, and a large strain of 0.35% with $S_{\text{max}}/E_{\text{max}}=471$ pm/V is achieved at the critical composition $x=0.03$, owing to the shift of the ferroelectric-to-relaxor transition temperature $T_{\text{F-R}}$ to ambient temperature. Intriguingly, the established correlation between strain response and $T_{\text{F-R}}$ demonstrates that the optimization of strain behavior of BNT-based ceramics can be realized through the regulation of $T_{\text{F-R}}$ to room temperature. Furthermore, a high and thermally stable electrostrictive coefficient Q_{33} of 0.018 m⁴/C² can also be attained at the composition $x=0.06$. In this study, it is believed that the modulation of phase transition temperature is feasible to achieve the large strain response in BNT-based ceramics.

1 Introduction

Piezoelectric ceramics have been widely used in electronic devices, such as actuators, sensors, and transducers, among which Pb-based Pb(Zr,Ti)O₃ (PZT) ceramics have governed the piezoelectric market owing to excellent piezoelectric performance [1, 2]. However, given that the lead element is volatile and toxic, the replacement of PZT materials is imperative [3]. Consequently, considerable effort has been devoted to the search for environment-free lead-free piezoelectric materials with performance comparable to PZT [4, 5]. To date, numerous research works are mainly focused on

BaTiO₃(BT)-, (Bi_{0.5}Na_{0.5})TiO₃ (BNT)-, and K_{0.5}Na_{0.5}NbO₃ (KNN)-based perovskite-structured ceramics [1]. Among reported lead-free piezoelectric ceramics, BNT-based ceramics have been deemed as the most likely materials to replace lead-based materials in actuator applications due to their giant field-induced strain response [6–8].

At present, (Bi_{0.5}Na_{0.5})TiO₃–BaTiO₃ (BNT–BT) and (Bi_{0.5}Na_{0.5})TiO₃–(Bi_{0.5}K_{0.5})TiO₃ (BNT–BKT) solid solutions have been confirmed to exhibit high strain at the morphotropic phase boundary (MPB) composition [5, 6, 9–16]. For example, Zhang et al. report a high strain of 0.45% in the Bi_{0.5}Na_{0.5}TiO₃–BaTiO₃–K_{0.5}Na_{0.5}NbO₃ (BNT–BT–KNN) pseudoternary solid solution system [6]. A large strain of 0.6% is obtained at 70 kV/cm by doping 2.5% LiNbO₃ into BNT–BT ceramics [5]. Wang et al. achieve a large unipolar strain of 0.36% with $S_{\text{max}}/E_{\text{max}}=600$ pm/V in the SrTiO₃-modified BNT–BKT ceramics [16]. Nevertheless, the current potential mechanism for high strain still remains controversial. Tan et al. indicate that the reason for the high strain should be attributed to the transformation of the field-induced antiferroelectric (AFE) to the ferroelectric (FE) phase together with the contribution of domain switching [6]. On the other hand, Hussain et al. propose that the high strain is caused by the coexistence of ferroelectric and non-polar phases at room temperature [17]. Herein, the

✉ Wangfeng Bai
bwfcxj@126.com

✉ Peng Zheng
zhengpeng@hdu.edu.cn

✉ Jiwei Zhai
apzhai@tongji.edu.cn

¹ College of Electronics and Information, Hangzhou Dianzi University, Hangzhou 310018, China

² College of Materials and Environmental Engineering, Hangzhou Dianzi University, Hangzhou 310018, China

³ Functional Materials Research Laboratory, School of Materials Science & Engineering, Tongji University, No. 4800 Caoan Highway, Shanghai 201804, China

elucidation of the mechanism for the giant strains is still worthy of continuous investigation.

In the design of the high-strain ceramics, the selected base composition should have a large strain. Moreover, the long-range ferroelectric order of the base composition can be disrupted readily with the help of chemical modifiers under high fields [18, 19]. Considering the rhombohedral (*R*) and tetragonal (*T*) phase coexistence when BNT and BT matrix are mixed [5, 20], BNT–BT solid solution may be an excellent choice for the base composition. Among developed $(1-x)\text{BNT}-x\text{BT}$ piezoelectric solid solution, 0.94BNT–0.06BT, which is a *R*–*T* MPB composition [1, 2, 4], exhibits high piezoelectric properties and depolarization temperature. In fact, this composition has frequently been the starting point for the production of many other piezoelectric ceramics with large strain response [6–10]. Therefore, we have chosen the MPB composition 0.94BNT–0.06BT as the base composition. BiScO₃ (BS) is a rhombohedral ferroelectric material, which has positive effects on electrical properties of BNT ceramics [21, 22]. It is expected to introduce BS into the BNT–BT to construct a ternary solid solution to tailor strain response.

In this study, a schematic phase diagram has been established to clarify the relationship between strain behavior and structure evolution. A large strain of 0.35% with $S_{\text{max}}/E_{\text{max}} = 471 \text{ pm/V}$ is realized at the critical composition $x = 0.03$. Furthermore, large and temperature-insensitive electrostriction coefficient Q_{33} at the composition $x = 0.06$ has also been gained. These results indicate that the studied material has great potential in practical actuator applications.

2 Experimental

The material $(1-x)(0.94\text{BNT}-0.06\text{BT})-x\text{BS}$ (BNT–BT–BS, $x = 0-0.06$) has been prepared by the conventional solid-state reaction method. The raw materials of high-purity Bi₂O₃

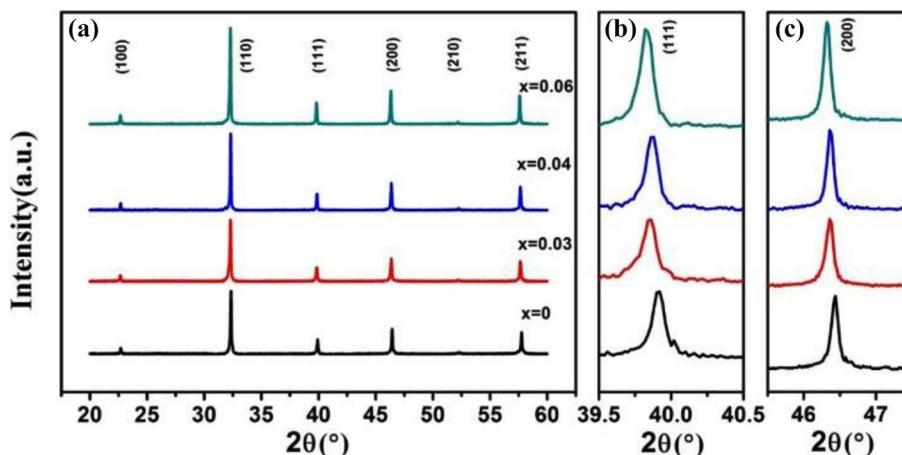
(99.975%), Na₂CO₃ (99.8%), TiO₂ (99.6%), BaCO₃ (99.8%), and Sc₂O₃ (99%) are weighed based on the stoichiometric formula. The mixtures are ball-milled for 6 h in ethanol and then the dried materials are calcined at 850 °C for 4 h. After the second ball-milled, the powders are pressed into pellets with a diameter of 10 mm by 8 wt% polyvinyl alcohol (PVA) as binder. The samples are buried in powder of the same composition to inhibit the volatilization of Bi and Na and then sinter at 1150 °C for 2 h. Silver electrodes are coated on both sides of the polished pellets and fired at 600 °C for 30 min for the electric measurement.

The phase structure of BNT–BT–BS ceramics is examined by using X-ray diffraction (XRD; 26 MiniFlex 600, Rigaku, Japan). The surface morphologies and element mapping of the samples are revealed by a scanning electron microscopy (SEM) (JSM, EMP-800; JEOL, Tokyo, Japan). The temperature dependence of dielectric constant and loss for the poled specimens are measured using High-precision LCR meter (HP 4990 A; Agilent, Palo Alto, CA) in the frequency range of 1–500 kHz. The electric field-induced polarization (*P*–*E*) loops and strain curves are performed at 10 Hz by means of a ferroelectric analyzer (TF Analyzer 2000, aixACCT Systems GmbH, Aachen, Germany) with a laser interferometer (SP-S120/500, SIOS Mebtechnik GmbH, Jena, Germany). The specimens for piezoelectric measurements are poled in silicone oil bath alone with a DC field of 50 kV/cm for 20 min. After 24-h aging of the poled samples, the piezoelectric coefficient d_{33} is measured via a quasi-static d_{33} m (ZJ-3AN, China).

3 Results and discussion

The XRD patterns of the BNT–BT–BS ceramics are shown in Fig. 1a, revealing a single perovskite structure without observable secondary phase. This result demonstrates that the BS has been successfully diffused into the BNT–BT

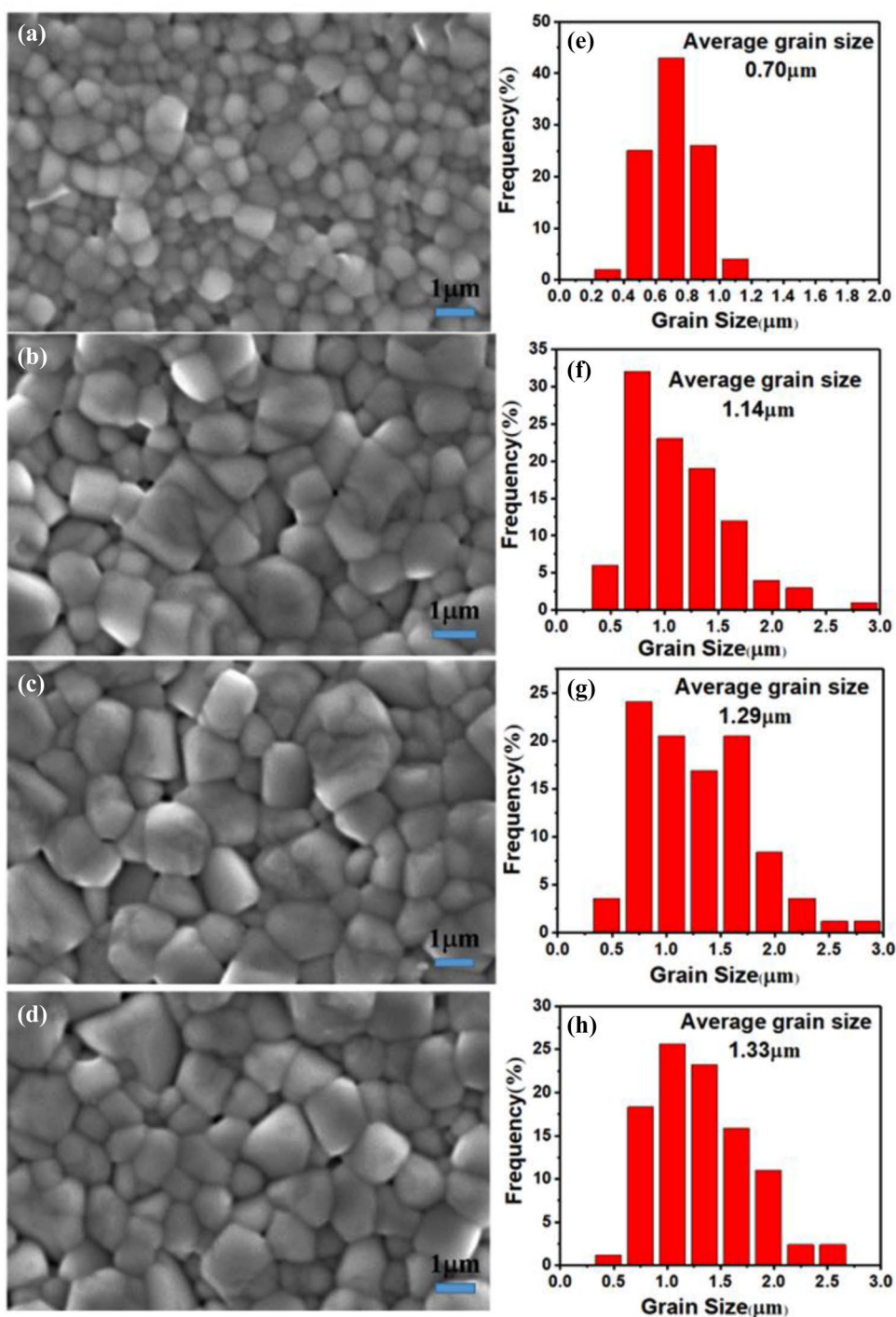
Fig. 1 a XRD patterns of BNT–BT–BS ceramics, and enlarged XRD profiles of **b** (111) and **c** (200) diffraction peaks



lattice and stable solid solution has been formed. Figure 1b and c displays the enlarged local XRD patterns of (111) and (200) peaks. No distinct peaks splitting can be observed, which manifests that all compositions behave as the pseudocubic phase [23]. On the other hand, it is also observed that the (111) and (200) diffraction peaks shift to lower diffraction angles as the BS content increases, indicating the tendency of a lattice expansion.

Figure 2 shows the SEM micrographs and grain size distribution of the investigated ceramics. As shown in Fig. 2a–d, all ceramics are well sintered and show dense morphologies. It can be observed that the introduction of BS has no obvious effects on the grain morphology of BNT–BT ceramics, most of which are the rectangular or square shape. Furthermore, as the doping content of BS increases, the average grain size increases continuously. This phenomenon

Fig. 2 SEM morphologies and grain size distribution of $(1-x)(0.94\text{BNT}-0.06\text{BT})-x\text{BS}$ ceramics: (a and e) $x=0$, (b and f) $x=0.03$, (c and g) $x=0.04$ and (d and h) $x=0.06$



can be explained by the process of liquid phase sintering. During the sintering process, extra Bi_2O_3 forms liquid phase and acts as a sintering aid at the high temperature, accelerating the dissolution and growth of grains [24–26].

The element mapping of $x = 0.03$ ceramic samples is measured and the results are showed in Fig. 3. Obviously, all the elements are evenly distributed throughout the ceramics. In addition, energy-dispersive X-ray spectroscopy (EDS) can be used to analyze the chemical compositions of the ceramics, as shown in Fig. 3b. All the elements are detected and the experimental data of each element is within the error of the theoretical value.

Figure 4 shows the temperature-dependent dielectric constant and loss for poled BNT–BT–BS ceramics at different

measurement frequencies. The curves for all the ceramics present two dielectric anomalies: a hump at lower temperature with strong frequency-dependent dispersion and a peak at higher temperature accompanied with a maximum of dielectric constant. The high temperature corresponding to the maximum dielectric permittivity can be defined as T_m , which is related to the tetragonal polar nanoregions (PNRs) relaxation generated from rhombohedral PNRs [16]. The other lower temperature (T_{F-R}) is attributed to the transition from ferroelectric-to-ergodic relaxor (FE-to-ER) state [16, 27, 28]. Scrutinizing on the dielectric responses, we can clearly see that T_m is almost unchanged with increasing BS content, whereas the T_{F-R} shifts to lower temperature. In detail, the T_{F-R} is approximately located at 79 °C

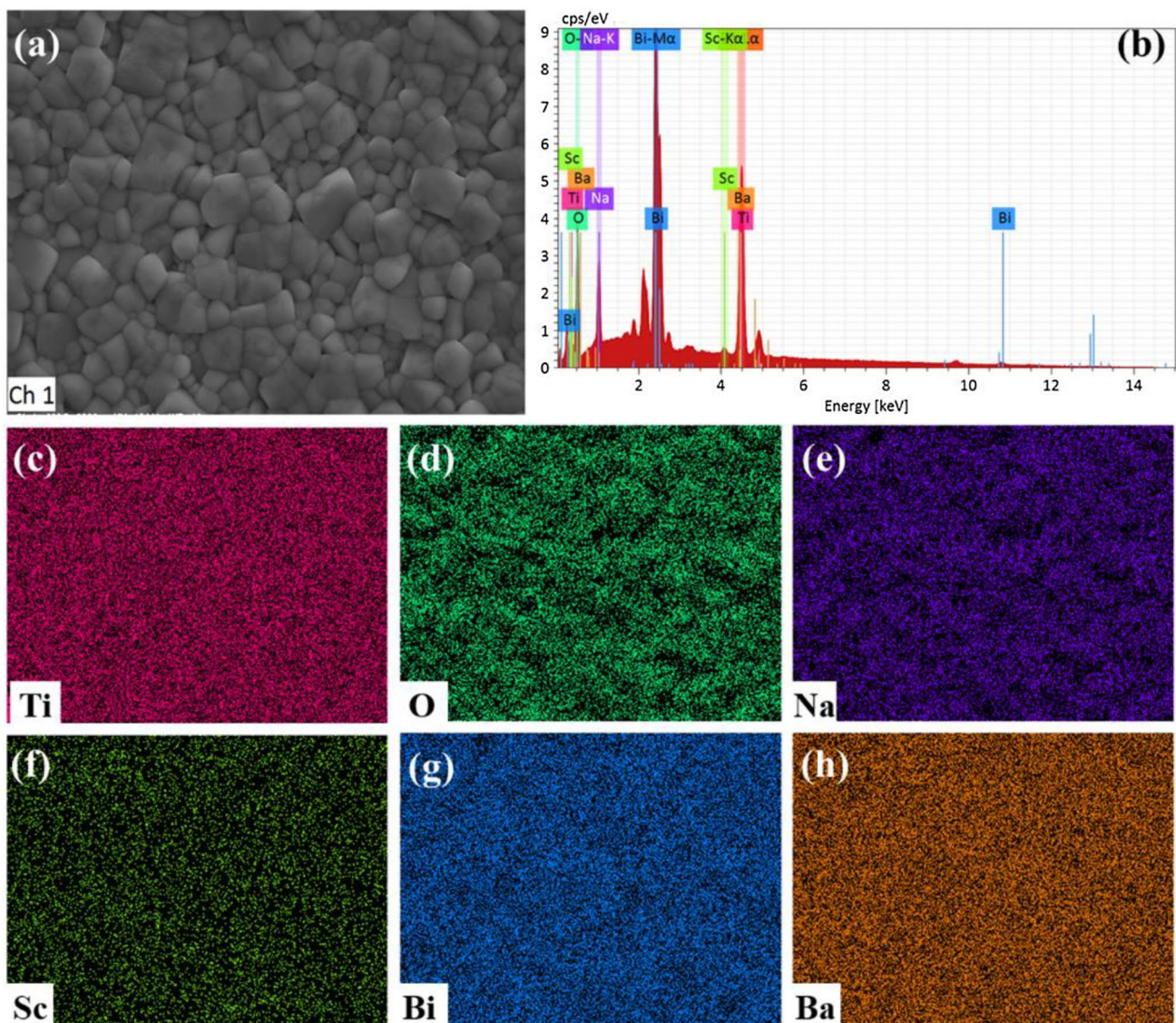


Fig. 3 Element mapping of the $x = 0.03$ ceramics: **a** SEM micrograph, **b** EDS data of the studied area. Element distribution of **c** Ti, **d** O, **e** Na, **f** Sc, **g** Bi and **h** Ba

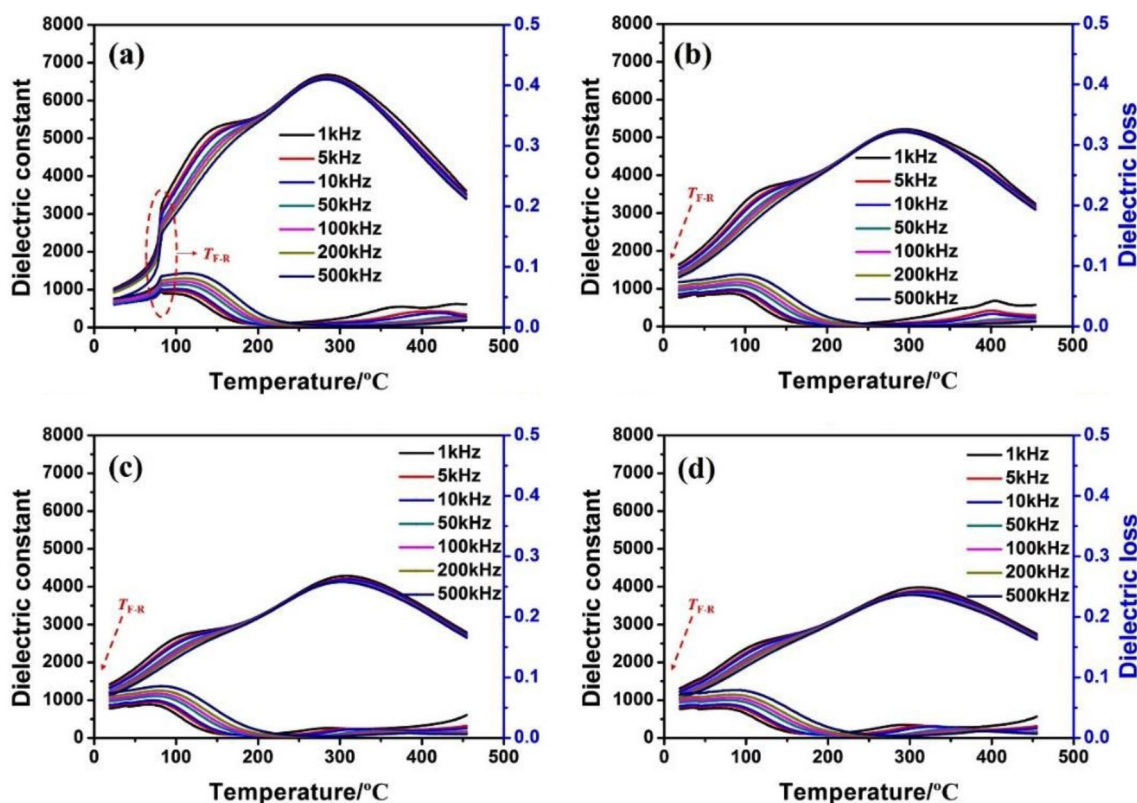


Fig. 4 Temperature dependence of dielectric constant and loss for poled $(1-x)(0.94\text{BNT}-0.06\text{BT})-x\text{BS}$ ceramics: **a** $x=0$, **b** $x=0.03$, **c** $x=0.04$, and **d** $x=0.06$

for BNT–BT ceramics, and then $T_{\text{F-R}}$ cannot be accurately detected for the compositions with $x=0.03-0.06$, which indicates that the $T_{\text{F-R}}$ has been reduced to room temperature [15, 16]. This phenomenon certifies that the ferroelectric-to-relaxor phase transition is completed by introducing BS into BNT–BT ceramics. In addition, the long-term ferroelectric order after polarization cannot be maintained since the $T_{\text{F-R}}$ is adjusted to room temperature. From the change of the maximum dielectric constant, it is easy to note that the dielectric constant decreases as the content of BS increases, which may be ascribed to compositionally induced ferroelectric-to-diffused phase transition [29].

It is well known that impedance spectroscopy can be used to investigate defect types and conductivity and clarify the influence of grain, grain boundary, and electrode interfaces on the conductive behavior of ceramics [30–33]. The corresponding complex impedance spectra for the different unpoled compositions are measured at temperatures ranging from 400 to 600 °C, as given in Fig. 5a–d. Obviously, the electron and oxygen ions are the main contribution factors of conductivity [34], as confirmed by the single semi-circles. In the complex impedance plane, the resistance is acquired by extrapolating the low-frequency intercept in the real axis [33]. Through the equivalent circuit (seeing

the inset in Fig. 5a), the resistors can be estimated by using Z-View software, as shown in Table 1. From the resistance values in Table 1, the resistance decreases as the temperature increases, indicating that the resistance exhibits a negative temperature coefficient.

In order to reveal the defect types of all investigated ceramics, the activation energy (E_a) for electrical conduction is detected by using the Arrhenius law:

$$\delta = \delta_0 \exp(-E_a/\kappa T),$$

where δ_0 represents a constant, κ means the Boltzmann constant, and T is an absolute temperature. Figure 5e displays the plot of $\ln(1/R)$ vs. $1000/T$. The corresponding E_a for BNT–BT– x BS ceramics are calculated to be 1.56 eV, 1.67 eV, 1.64 eV, and 1.48 eV, respectively. It is easy to conclude that the E_a of the component with $x=0.03$ is enhanced in relative to BNT–BT ceramics, indicating that the concentration of oxygen vacancies is reduced [33, 35]. Fundamentally, the generation of oxygen vacancies will limit the movement of the domain walls, resulting in deterioration of the electrical properties [36]. Therefore, we can infer that ceramics-doped BS content of 3 mol% may have excellent performance.

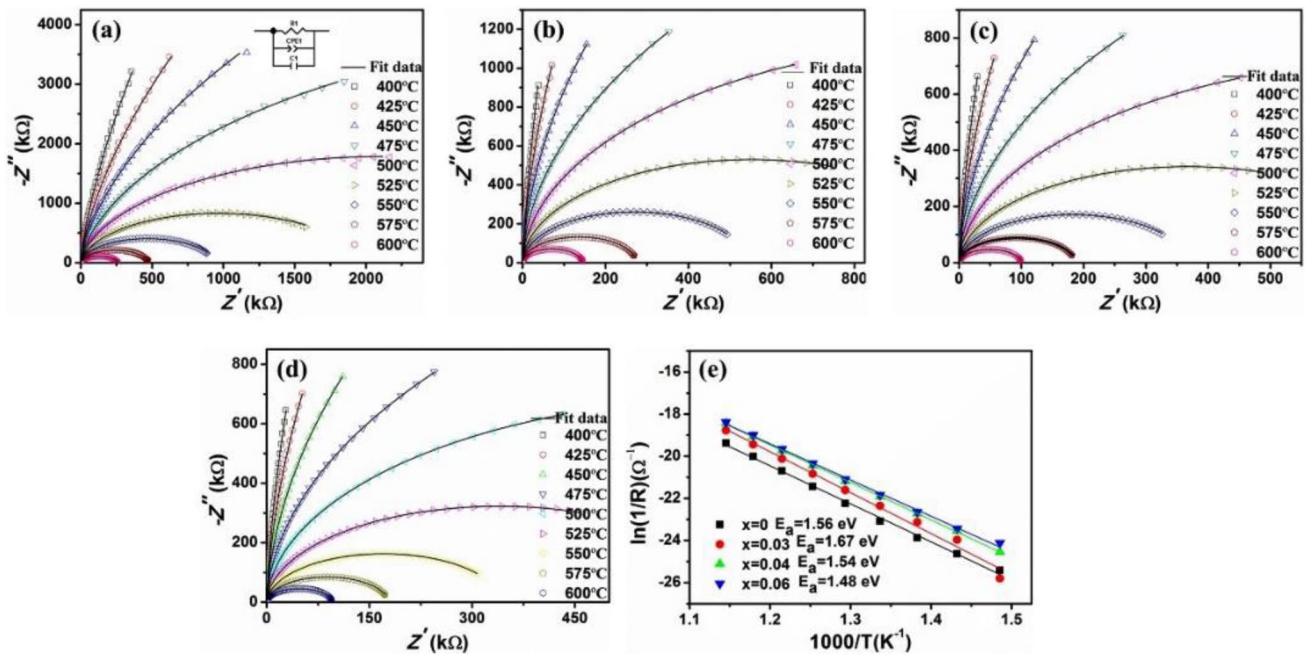


Fig. 5 Complex impedance spectra of BNT–BT– x BS ceramics: **a** $x=0$, **b** $x=0.03$, **c** $x=0.04$, **d** $x=0.06$. The inset shows the RC equivalent circuit for all samples. **e** Plot of $\ln(1/R)$ vs. $1000/T$ of all investigated samples

Table 1 Fitting parameters of impedance data for all the compositions at various temperatures

Measuring temperatures (°C)	$x=0$	$x=0.03$	$x=0.04$	$x=0.06$
	R_1 (kΩ)	R_1 (kΩ)	R_1 (kΩ)	R_1 (kΩ)
400	108,600	159,400	45,614	30,020
425	50,114	25,612	16,775	15,195
450	23,395	11,012	7351	6858
475	10,543	5087	3291	3062
500	4534	2429	1598	1464
525	2033	1120	755	691
550	970	548	372	346
575	490	277	190	179
600	262	142	101	96

The ferroelectric hysteresis loops and the corresponding current-field curves of BNT–BT–BS ceramics are measured at room temperature, as exhibited in Fig. 6a and b. We observe easily that BNT–BT ceramics exhibit a well-saturated and square hysteresis loops along with sharp current peaks in current-field curves, reflecting the nature of ferroelectricity. With the addition of BS, the polarization hysteresis loops are squeezed together with the decrease of the remnant polarization P_r and coercive field E_c . At the same time, the sharp current peak gradually becomes broadening, which is ascribed to the transition from an electric field-induced relaxor to ferroelectric phase. For further investigating the structure evolution, the field-dependent small signal

piezoelectric coefficient $d_{33}(E)$ are measured at 70 kV/cm, as presented in Fig. 6c. In general, we define the positive value of the zero electric field in the $d_{33}(E)$ curve as the small signal piezoelectric coefficient $d_{33}(E)$ [37–39]. Obviously, as the BS content increases, the small signal d_{33} continuously decreases, indicating that the ferroelectricity of ceramics is constantly weakened. This observation conforms to the change in the corresponding polarization hysteresis loops (Fig. 6a) and field-current curves (Fig. 6b).

The bipolar and unipolar strain curves of investigated samples are also measured at 75 kV/cm, as shown in Fig. 6d and e, respectively. The composition-driven ferroelectric-to-relaxor phase transition can also be demonstrated by the corresponding strain curves, just like the hysteresis loops (Fig. 6a–c). BNT–BT ceramics exhibit butterfly-shaped with obvious negative strain (0.19%) and quasi-linear with small hysteresis strain loops, revealing the ferroelectric nature of the ceramics. In contrast, we can observe that a typical butterfly shape has transformed into a sprout-shaped one with tiny negative strain for BNT–BT–0.03BS ceramics, suggesting the coexistence of the ferroelectric phase and relaxor phase. Hence, this critical composition exhibits a maximum strain (0.35%) with pronounced hysteretic behavior. Similar phenomenon has also been observed in other various BNT-based ceramics [5, 6, 15, 16, 40]. At the compositions $x > 0.03$, negative strain has not been detected and the curve is seriously contracted, which reveals the disappearance of ferroelectric order and the emergence of relaxor phase. Figure 6f presents the dynamic dielectric constant

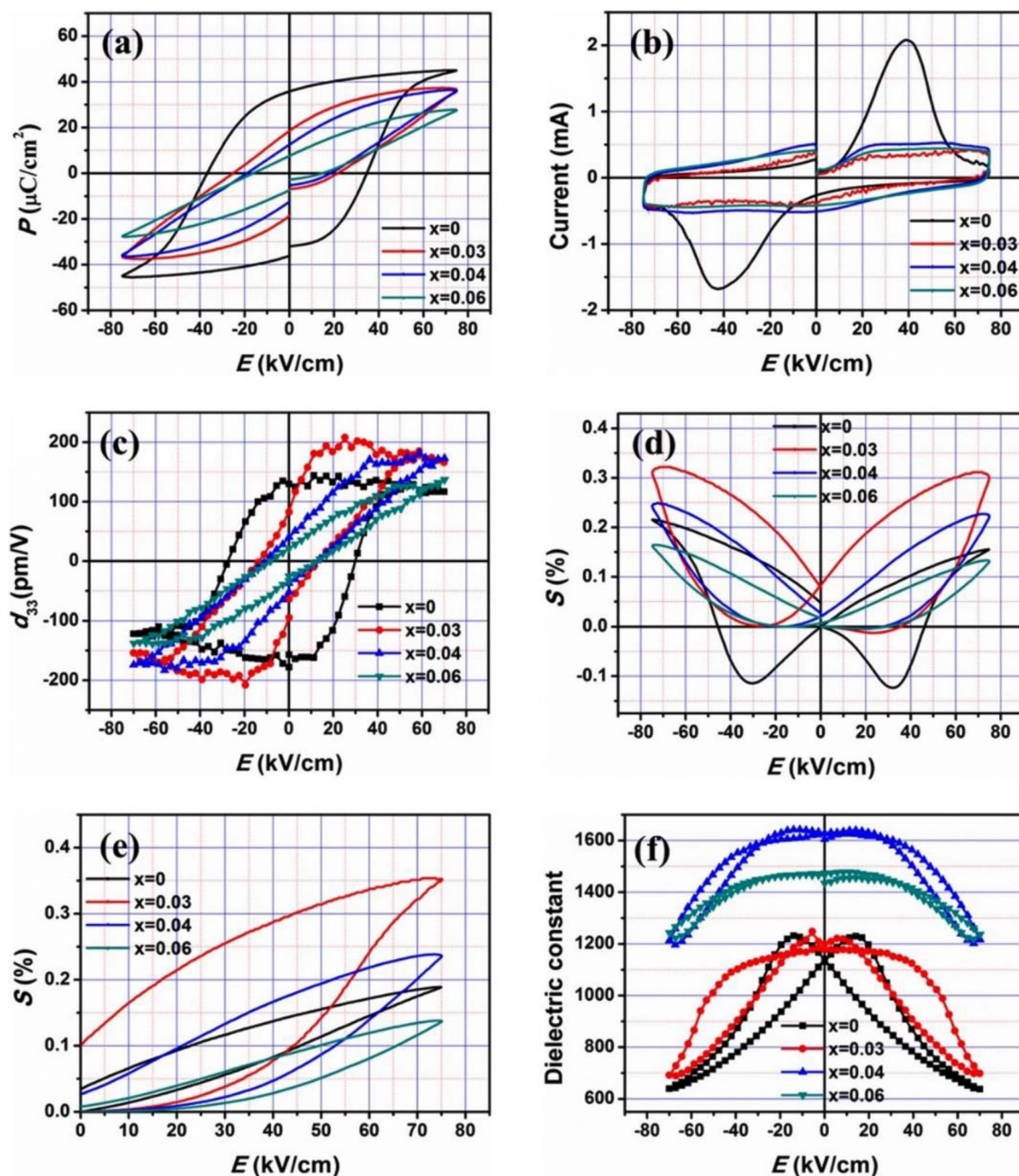


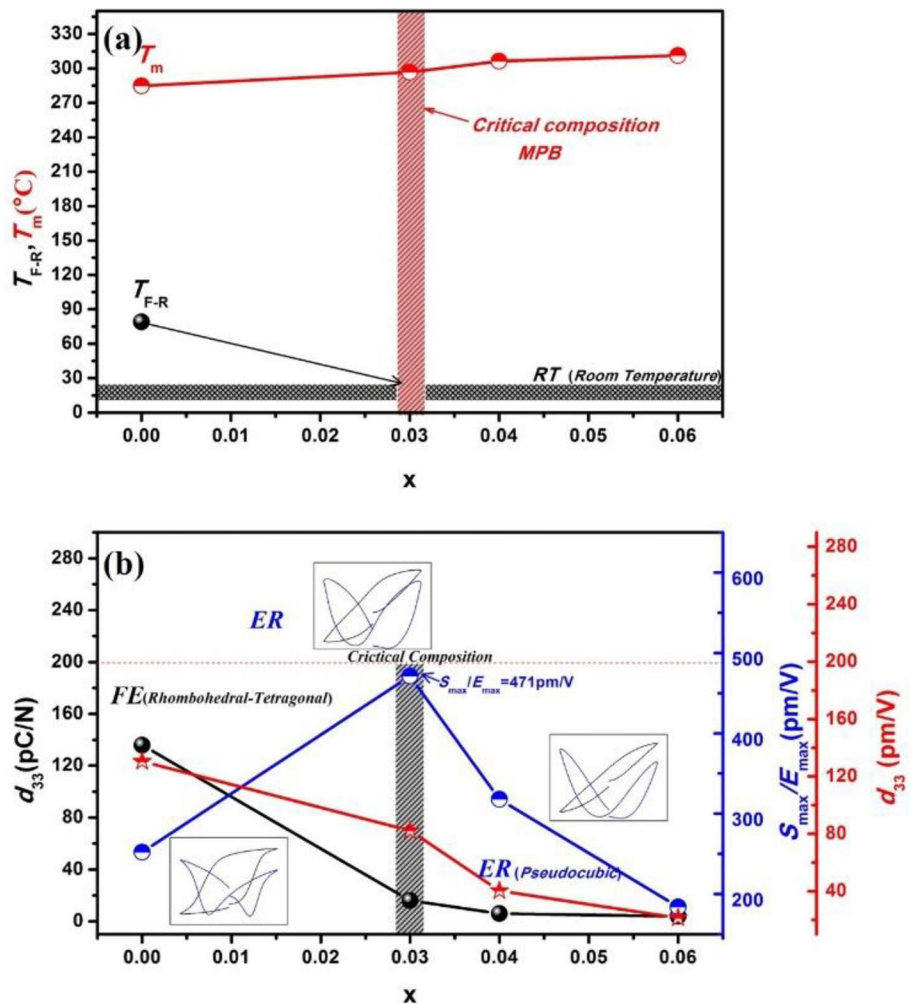
Fig. 6 **a** Polarization hysteresis loops, **b** polarization current curves, **c** small signal d_{33} , **d** bipolar strain curves, **e** unipolar strain curves, and **f** dynamic dielectric constant for the BNT–BT–BS ceramics

of BNT–BT– x BS ceramics to explore the structure evolution. As the BS content increases, the shape of the dynamic dielectric constant changes significantly. Analogous to the observation in bipolar strain curves, there is a hysteresis in the dynamic dielectric constant for undoped BS sample, and the local maximum value in the curve appears near the coercive field as a result of the field-induced domain reorientations [41, 42]. With the introduction of BS into BNT–BT ceramics, the local maximum gradually spread and

the hysteresis decreases, further confirming the BS-driven phase transition.

Based on the investigated structure evolution and dielectric, piezoelectric, and electromechanical properties measurements, a schematic phase diagram for the BNT–BT–BS system is constructed and displayed in Fig. 7a. It can be seen that the T_{F-R} has been adjusted to below room temperature when the doped BS content reaches 3 mol%. This verifies the phase coexistence between ferroelectric and relaxor phases

Fig. 7 **a** The schematic phase diagram of BNT–BT–BS ceramics, **b** d_{33} , S_{\max}/E_{\max} , and small signal $d_{33}(E)$ as a function of BS content



for the critical composition, giving rise to the generation of large strain response (Fig. 6e). Figure 7b presents the d_{33} , normalized strain S_{\max}/E_{\max} , and small signal $d_{33}(E)$ as a function of BS content for the indicated ceramics. There is a clear trade-off between the d_{33} and S_{\max}/E_{\max} value. The d_{33} has a maximum value of 136 pC/N for BNT–BT ceramics, then drops sharply to 16 pC/N at the critical composition $x = 0.03$, and finally remains at a very low value. Meanwhile, the S_{\max}/E_{\max} behaves a sudden fluctuation ($d_{33} = 471 \text{ pm/V}$) at the critical composition $x = 0.03$. On the other hand, the $d_{33}(E)$ shows the similar trend as d_{33} with increasing BS content, which reveals the existence of same physical origin between d_{33} and $d_{33}(E)$.

To verify the effect of electric field on the phase transition of the BNT–BT–0.03BS ceramics, XRD patterns before and after poling are compared in Fig. 8. In the unpoled specimens, there is no peak splitting for the (111) and (200) peaks, which is a typical pseudocubic structure [43]. In the case of poled samples, the splitting of the (111) and (200) peaks appears, reflecting electric field-induced discernible non-cubic deformation. This attests the existence of different

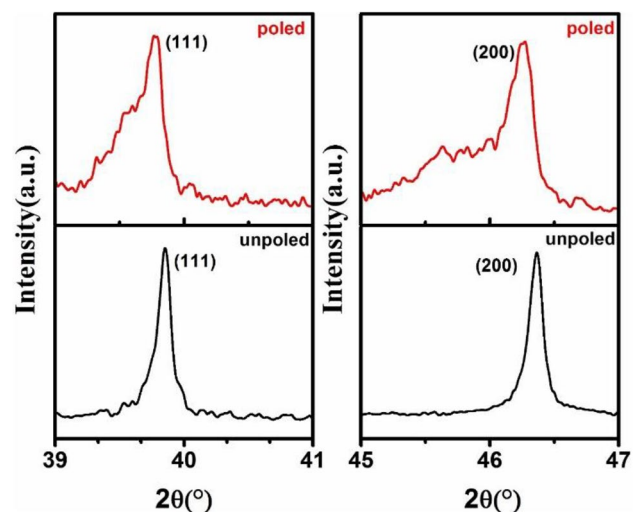


Fig. 8 XRD patterns of unpoled and poled BNT–BT–0.03BS ceramics

symmetries after poling (most likely rhombohedral–tetragonal mix phases) [44]. Herein, we can say poling treatment-driven the phase transition from the relaxor pseudocubic to the ferroelectric phases, which is the main source of the emergence of high electric field induced strain in the critical component $x=0.03$.

Temperature dependence of polarization hysteresis loops, bipolar strain curves, and unipolar strain curves for the ceramics with $x=0$, $x=0.03$, and $x=0.06$ are measured at 60 kV/cm under different temperatures, as shown in Fig. 9. The pure BNT–BT ceramics exhibit typical ferroelectric characteristic at room temperature. At above 70 °C, the polarization hysteresis loops become clamped and the shape of strain curves changes to sprout-shaped ones, showing the temperature-induced phase transition. For the BNT–BT–0.03BS composition, due to the coexistence of ferroelectric and relaxor phases at room temperature, the polarization hysteresis loops behave pinching and the

bipolar field strain exhibits the maximum at room temperature. As the temperature increases, a monotonous reduction in strain value is observed in the whole temperature range. The $x=0.06$ composition possesses the complete ergodic relaxor phase (Fig. 5), resulting in the appearance of very slim hysteresis loops and remarkable sprout-shaped bipolar strain curves [45]. In summary, similar to the effect of composition (Fig. 6), increasing temperature can also drive phase transition between ferroelectric and relaxor phases.

Figure 10 shows the d_{33}^* as a function of temperature for the investigated samples. From the degree of fluctuation of d_{33}^* for each component with respect to temperature, we can find that d_{33}^* of the $x=0.06$ composition varies from a minimum of 138 pm/V at 27 °C to a maximum of 156 pm/V at 100 °C, exhibiting excellent temperature stability. This is ascribed to the situation that the component has complete relaxor phase at room temperature, as confirmed in Figs. 5 and 6. Figure 10b exhibits the

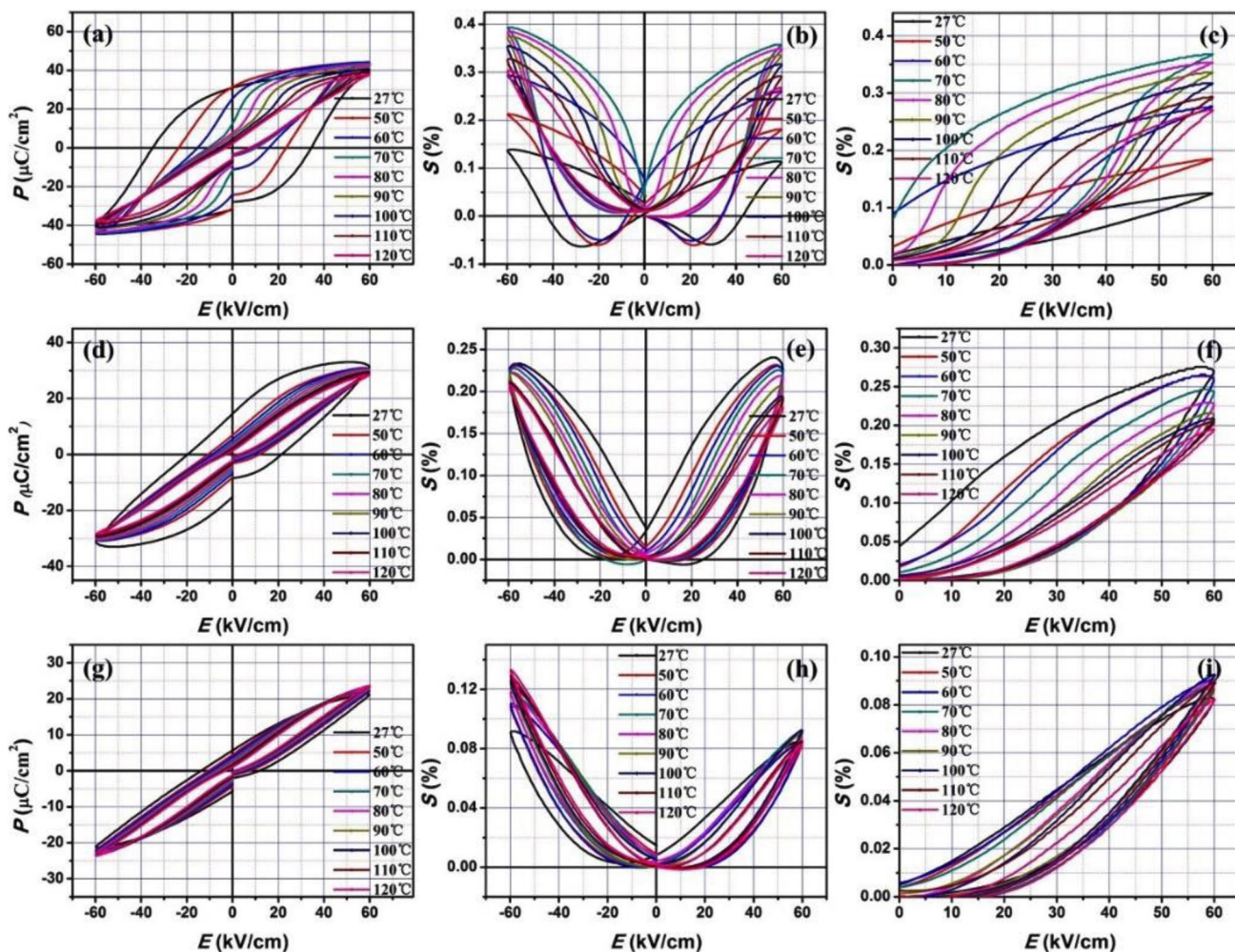


Fig. 9 Temperature dependence of polarization hysteresis loops (a, d and g), bipolar strain curves (b, e and h), and unipolar strain curves (c, f and i) for the ceramics with $x=0$, 0.03, and 0.06

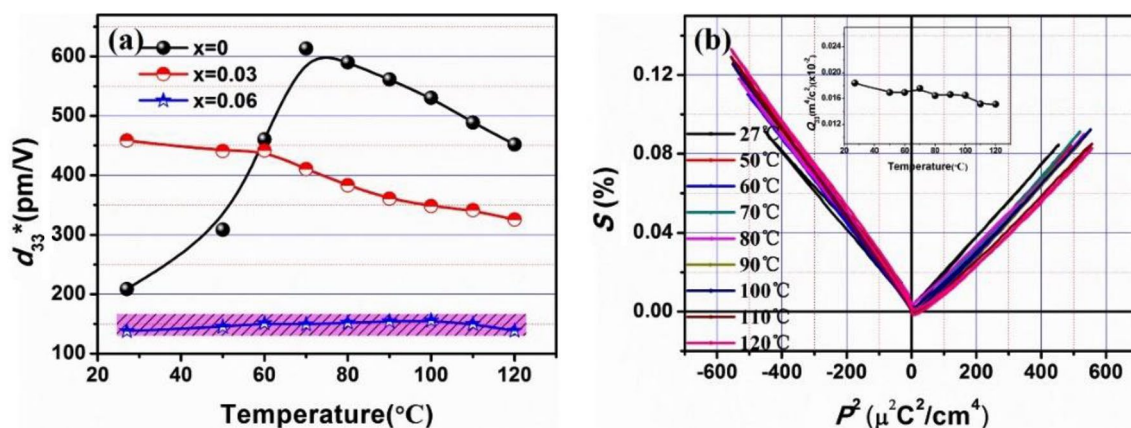


Fig. 10 **a** d_{33}^* as a function of temperature for the ceramics with $x=0$, $x=0.03$ and $x=0.06$, **b** temperature-dependent S - P^2 plot for BNT-BT-0.06BS ceramics. The inset shows the corresponding Q_{33} with respect to temperature

strain versus polarization squared (P^2) curve, and the Q_{33} is obtained from the slope of these curves. Apparently, phenomenologically electrostrictive characteristic can be found in the BNT-BT-0.06BS ceramics, evidenced by a strongly linear dependence with the polarization squared [8, 42, 46]. The Q_{33} is determined to be $\sim 0.018 \text{ m}^4/\text{C}^2$ at room temperature and maintains excellent stability against temperature change (seeing the inset of Fig. 10b), which might be due to the presence of ferroelectric nanodomains [47, 48]. This value is not less than $0.017 \text{ m}^4/\text{C}^2$ of the representative electrostrictive material PMN [49]. The achieved large and temperature-insensitive Q_{33} in BS-modified BNT-BT ceramics offers great potential in the precision position control devices aspect.

4 Conclusions

In this study, we construct the BNT-BT-BS ternary solid solution and realize a high strain response of 0.35% ($S_{\max}/E_{\max} = 471 \text{ pm/V}$) at the critical composition $x=0.03$. In view of the measured structure evolution and ferroelectric, dielectric, and electromechanical properties, a phase diagram is established and the correlation between the phase structure and electromechanical performance is clarified. Introducing BS causes the phase transformation from relaxor pseudocubic to ferroelectric phases, producing the pinch-shaped hysteresis loops and the sprout-shaped bipolar strain curves. Furthermore, the composition $x=0.06$ behaves a large and temperature-insensitive Q_{33} ($\sim 0.018 \text{ m}^4/\text{C}^2$), which provides a fresh solution to promote the electrostrictive behavior. Hence, these results in this work will be helpful to further understand the positive effects of BS on the strain response and the intrinsic relation between physical structure and electromechanical response of BNT-related ceramics.

Acknowledgements The authors would like to acknowledge the National Natural Science Foundation of China (Grant No. 51502067), Natural Science Foundation of Zhejiang Province (LQ16E020004), key research, and development projects of Zhejiang Province (2017C01056).

References

1. J. Hao, W. Li, J. Zhai, H. Chen, *Mater. Sci. Eng. R.* **135**, 1–57 (2019)
2. T. Zheng, J. Wu, D. Xiao, J. Zhu, *Prog. Mater. Sci.* **98**, 552–624 (2019)
3. E. Cross, *Nature* **432**, 24 (2004)
4. J. Rödel, W. Jo, K.T.P. Seifert, E.-M. Anton, T. Granzow, D. Damjanovic, *J. Am. Ceram. Soc.* **92**, 1153–1177 (2009)
5. J. Chen, Y. Wang, Y. Zhang, Y. Yang, R. Jin, *J. Eur. Ceram. Soc.* **37**, 2365–2371 (2017)
6. S.-T. Zhang, A.B. Kounga, E. Aulbach, H. Ehrenberg, J. Rödel, *Appl. Phys. Lett.* **91**, 112906 (2007)
7. W. Jo, R. Dittmer, M. Acosta, J. Zang, C. Groh, E. Sapper, K. Wang, J. Rödel, *J. Electroceram.* **29**, 71–93 (2012)
8. S.-T. Zhang, A.B. Kounga, W. Jo, C. Jamin, K. Seifert, T. Granzow, J. Rodel, D. Damjanovic, *Adv. Mater.* **21**, 4716–4720 (2009)
9. Y. Guo, Y. Liu, R.L. Withers, F. Brink, H. Chen, *Chem. Mater.* **23**, 219–228 (2010)
10. F. Wang, M. Xu, Y. Tang, T. Wang, W. Shi, C.M. Leung, J. Rödel, *J. Am. Ceram. Soc.* **95**, 1955–1959 (2012)
11. X. Liu, X. Tan, *J. Appl. Phys.* **120**, 034102 (2016)
12. J. Hao, Z. Xu, R. Chu, W. Li, J. Du, G. Li, *J. Phys. D* **48**, 472001 (2015)
13. H. Zhang, P. Xu, E. Patterson, J. Zang, S. Jiang, J. Rödel, *J. Eur. Ceram. Soc.* **35**, 2501–2512 (2015)
14. S.-T. Zhang, B. Yang, W. Cao, *Acta Mater.* **60**, 469–475 (2012)
15. W. Bai, D. Chen, Y. Huang, B. Shen, J. Zhai, Z. Ji, *J. Alloys Compd.* **667**, 6–17 (2016)
16. K. Wang, A. Hussain, W. Jo, J. Rödel, D.D. Viehland, *J. Am. Ceram. Soc.* **95**, 2241–2247 (2012)
17. A. Hussain, C.W. Ahn, J.S. Lee, A. Ullah, I.W. Kim, *Sens. Actuators A* **158**, 84–89 (2010)
18. T. Li, X. Lou, X. Ke, S. Cheng, S. Mi, X. Wang, J. Shi, X. Liu, G. Dong, H. Fan, Y. Wang, X. Tan, *Acta Mater.* **128**, 337–344 (2017)

19. W. Jo, T. Granzow, E. Aulbach, J. Rödel, D. Damjanovic, J. Appl. Phys. **105**, 094102 (2009)
20. W. Jo, J. Daniels, D. Damjanovic, W. Kleemann, J. Rödel, Appl. Phys. Lett. **102**, 192903 (2013)
21. P. Marchet, E. Boucher, V. Dorcet, J.P. Mercurio, J. Eur. Ceram. Soc. **26**, 3037–3041 (2006)
22. Y. Hiruma, H. Nagata, T. Takenaka, Appl. Phys. Lett. **95**, 052903 (2009)
23. A. Hussain, A. Maqbool, R.A. Malik, I. Qazi, T.-K. Song, W.-J. Kim, M.-H. Kim, Phys. Status Solidi A **215**, 1700942 (2018)
24. H. Ogihara, C.A. Randall, S. Trolier-McKinstry, J. Am. Ceram. Soc. **92**, 110–118 (2009)
25. G. Dong, H. Fan, J. Shi, Q. Li, J. Am. Ceram. Soc. **101**, 3947–3955 (2018)
26. S. Gao, Z. Yao, L. Ning, G. Dong, H. Fan, Q. Li, Adv. Eng. Mater. **19**, 1700125 (2017)
27. W. Jo, S. Schaab, E. Sapper, L.A. Schmitt, H.-J. Kleebe, A.J. Bell, J. Rödel, J. Appl. Phys. **110**, 074106 (2011)
28. D.-S. Yin, Z.-H. Zhao, Y.-J. Dai, Z. Zhao, X.-W. Zhang, S.-H. Wang, S. Zhang, J. Am. Ceram. Soc. **99**, 2354–2360 (2016)
29. A. Ullah, C. Won Ahn, A. Ullah, I. Won Kim, Appl. Phys. Lett. **103**, 022906 (2013)
30. S. Rout, S. Parida, E. Sinha, P. Barhai, I. Kim, Curr. Appl. Phys. **10**, 917–922 (2010)
31. I. Clark, F. Marques, D. Sinclair, J. Eur. Ceram. Soc. **22**, 579–583 (2002)
32. Z. Peng, X. Zeng, F. Cao, X. Yang, J. Alloys Compd. **695**, 626–631 (2017)
33. X.-Y. Geng, J. Zhang, R.-X. Wang, X.-Z. Deng, L. Sun, Z.-B. Gu, S.-T. Zhang, J. Am. Ceram. Soc. **100**, 5659–5667 (2017)
34. J. Shi, W. Tian, X. Liu, H. Fan, J. Am. Ceram. Soc. **100**, 1080–1090 (2017)
35. C. Tian, F. Wang, X. Ye, Y. Xie, T. Wang, Y. Tang, D. Sun, W. Shi, Scripta Mater. **83**, 25–28 (2014)
36. X. Yan, M. Zheng, S. Sun, M. Zhu, Y. Hou, Dalton Trans. **47**, 9257–9266 (2018)
37. W. Bai, L. Wang, P. Zheng, F. Wen, L. Li, J. Zhai, Z. Ji, Ceram. Int. **44**, 16040–16050 (2018)
38. F.-Z. Yao, Q. Yu, K. Wang, Q. Li, J.-F. Li, RSC Adv. **4**, 20062–20068 (2014)
39. J.-S. Zhou, K. Wang, F.-Z. Yao, T. Zheng, J. Wu, D. Xiao, J. Zhu, J.-F. Li, J. Mater. Chem. C **3**, 8780–8787 (2015)
40. K.T. Seifert, W. Jo, J. Rödel, J. Am. Ceram. Soc. **93**, 1392–1396 (2010)
41. Y. Zhang, D.C. Lupascu, E. Aulbach, I. Baturin, A. Bell, J. Rödel, Acta Mater. **53**, 2203–2213 (2005)
42. H.-S. Han, W. Jo, J.-K. Kang, C.-W. Ahn, I. Won Kim, K.-K. Ahn, J.-S. Lee, J. Appl. Phys. **113**, 154102 (2013)
43. H.S. Han, W. Jo, J. Rodel, I.K. Hong, W.P. Tai, J.S. Lee, J. Phys. Condens. Matter **24**, 365901 (2012)
44. W. Bai, D. Chen, Y. Huang, P. Zheng, J. Zhong, M. Ding, Y. Yuan, B. Shen, J. Zhai, Z. Ji, Ceram. Int. **42**, 7669–7680 (2016)
45. G. Dong, H. Fan, J. Shi, M. Li, W. Jo, J. Am. Ceram. Soc. **98**, 1150–1155 (2015)
46. C. Ang, Z. Yu, Adv. Mater. **18**, 103–106 (2006)
47. J. Kling, X. Tan, W. Jo, H.J. Kleebe, H. Fuess, J. Rödel, J. Am. Ceram. Soc. **93**, 2452–2455 (2010)
48. J. Shi, H. Fan, X. Liu, A.J. Bell, J. Am. Ceram. Soc. **97**, 848–853 (2014)
49. A. Furuta, K. Uchino, J. Am. Ceram. Soc. **76**, 1615–1617 (1993)

Publisher's Note Springer Nature remains neutral with regard to jurisdictional claims in published maps and institutional affiliations.